Article:
Zhu, L., Jiang, S.Z., Zhu, Z.Q. et al. (2009) Analytical modeling of open-Circuit air-Gap field distributions in multisegment and multilayer interior permanent-magnet machines. IEEE Transactions on Magnetics, 45 (8). pp. 3121-3130. ISSN: 0018-9464

https://doi.org/10.1109/TMAG.2009.2019841

Analytical Modeling of Open-Circuit Air-Gap Field Distributions in Multisegment and Multilayer Interior Permanent-Magnet Machines

Li Zhu[1], S. Z. Jiang[1], Z. Q. Zhu[2], *Fellow, IEEE*, and C. C. Chan[3], *Fellow, IEEE*

[1]Department of Electrical Engineering, Shanghai Jiao Tong University, Shanghai, China
[2]Department of Electronic and Electrical Engineering,University of Sheffield, Sheffield S1 3JD, U.K.
[3]Department of Electrical and Electronic Engineering, University of Hong Kong, Hong Kong

We present a simple lumped magnetic circuit model for interior permanent-magnet (IPM) machines with multisegment and multilayer permanent magnets. We derived analytically the open-circuit air-gap field distribution, average air-gap flux density, and leakage fluxes. To verify the developed models and analytical method, we adopted finite-element analysis (FEA). We show that for prototype machines, the errors between the FEA and analytically predicted results are $<1\%$ for multisegment IPM machines and $<2\%$ for multilayer IPM machines. By utilizing the developed lumped magnetic circuit models, the IPM machines can be optimized for maximum fundamental and minimum total harmonic distortion of the air-gap flux density distribution.

Index Terms—**Air-gap flux density, interior permanent magnet, leakage flux, multilayer, multisegment.**

I. Introduction

DUE to high efficiency, high power density, high power factor, and high torque density, together with the development of permanent-magnet (PM) material and power electronics, PM brushless machines are increasingly being used in various applications, such as variable-speed drives, servo drives, electric vehicles, and other industrial drives [1], [2]. Compared with surface-mounted PM (SPM) machines, interior permanent-magnet (IPM) synchronous machines have robust rotor construction, high reluctance torque, and high irreversible demagnetization withstand, and are eminently suitable for electric vehicles which require a wide constant power operating speed range.

However, due to significant leakage flux and magnetic saturation in IPM machines, it is very difficult to directly employ analytical methods to predict the open-circuit air-gap field distribution. Although the finite-element analysis (FEA) can precisely obtain the flux density distribution, it is time consuming and still often used only for design verification. Therefore, a lumped magnetic circuit model usually is a good compromise between simplicity and accuracy [3]–[9]. By way of examples, Laplacian or quasi-Poissonian field equations were directly solved analytically for SPM machines [10], [11] and inset PM machines [12], conformal mapping techniques were used for analyzing the influence of stator slotting [13]–[15] and rotor saliency in IPM machines [16], [17], while lumped magnetic circuit methods [3]–[9], [18]–[26] were extensively used for SPM machines [18]–[20], switched reluctance machines [21], linear brushless dc machines [22], hybrid stepping motors [5], salient-pole synchronous machines [23], flux-switching PM machines [24]–[26], inset PM machines [6], IPM machines [3], [4], [7]–[9], etc. In the lumped magnetic circuit analysis, the permeances of stator yoke and rotor yoke were often omitted for simplicity [5]–[7], [9], [18], [22], [25], [26], or handled with the nonlinear B-H curve of iron by iterative process for higher accuracy [3], [4], [8], [19]–[21], [23], [24]. However, since there is no significant magnetic saturation at yokes, neglecting the permeances of stator yoke and rotor yoke is usually acceptable and the results will still have fair accuracy [27]. To account for the slotting effect, [3], [6], [7] introduced Carter coefficient for predicting the average air-gap flux density, and [4], [5], [18], [20], [21], [24]–[26] analytically approximated the flux distributions in the slots by assuming straight and semicircular lines for predicting air-gap flux density distribution. However, the stator slots can be neglected if only the average air-gap flux density is considered [8], [9], [19], [23]. To investigate the end effect, a 3-D lumped magnetic circuit was employed in [20], [24], [25]. Furthermore, lumped magnetic circuits were also developed according to different rotor positions in order to account for rotor rotation [4], [5], [20], [21], [24], [26], much attention being paid to the nonlinear permeances in teeth [20] or pole tips [21], [24], [26] by employing iterative process [20], [21], [24] or by using saturated coefficients based on FEA [26]. Lumped magnetic circuits are particularly useful for IPM machines due to highly saturated rotor bridges and complicated rotor configurations. The rotor bridges could be modeled as constant flux leakage sources with preset values [6]–[8] or nonlinear permeance elements using iterative process [3], [4], [9]. Although the assumption in [6]–[8] might cause error since the saturation level of rotor iron bridge could be varied under different loading conditions, it was fairly acceptable for approximation as it resulted in significant simplification.

Hence, this paper presents improved lumped magnetic circuit models for analytically predicting the open-circuit air-gap flux density distributions in IPM machines with multisegment and multilayer permanent magnets. Based on the analysis of flux lines obtained by FEA, simplified lumped magnetic circuits are obtained and Kirchhoff's law is adopted for deriving the analytical expressions of the leakage fluxes. The influence of design parameters on the average air-gap flux density is investigated. The relationship between the lumped magnetic circuit models of different number of permanent-magnet layers is discussed. Furthermore, by utilizing the lumped magnetic circuit models, the

Manuscript received December 08, 2008; revised March 14, 2009. Current version published July 22, 2009. Corresponding author: Z. Q. Zhu (e-mail: z.q.zhu@sheffield.ac.uk).

Color versions of one or more of the figures in this paper are available online at http://ieeexplore.ieee.org.

Digital Object Identifier 10.1109/TMAG.2009.2019841

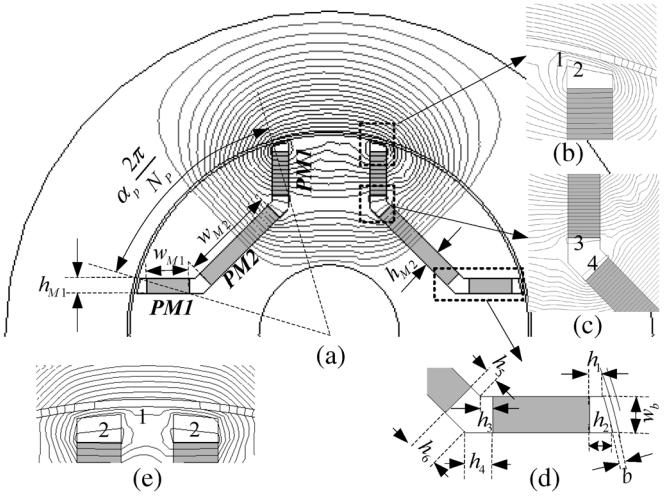

Fig. 1. IPM machine structure with multisegment permanent magnets.

IPM machines are optimized for maximum fundamental air-gap flux density [and electromotive force (EMF)], as well as minimum total harmonic distortion (THD) of air-gap flux density and EMF waveforms. FEA is used extensively to verify the developed models and analytical method.

II. Analytical Model for Multisegment IPM Machines

Although, in general, the influence of load and stator slotting can be easily accounted for in the lumped magnetic circuit [3]–[9], [18]–[26], in order to highlight the influence of rotor design parameters and provide a simple and useful means at early design stage, analytical models will be developed for multisegment IPM machines in this section and for multilayer IPM machines in the next section, both on open-circuit and assuming a smooth stator, i.e., neglecting the slotting effect.

Fig. 1 shows the IPM machine with multisegment permanent magnets, designated as $PM1$ and $PM2$. FEA predicted flux lines clearly show that the air-gap flux can be divided into two parts. One part is excited by $PM1$, and the other part is excited by $PM2$. Therefore, in Fig. 2, the actual air-gap flux density distribution, curve 1, is simplified to curve 2, where θ is the angle along the circumference, N_P is the number of magnet poles, α_p is the pole-arc to pole-pitch ratio, Fig. 1(a). In Fig. 1, the flux line 1 represents the leakage flux through the bridge and is excited by $PM1$. Flux lines 2 and 3 represent the magnet end-leakage fluxes in the slot for $PM1$. Flux line 4 represents the magnet end-leakage flux in the slot for $PM2$. Hence, Fig. 3(a) shows the lumped magnetic circuit associated with the fluxes excited by $PM1$. In Fig. 1(a), the leakage flux through the bridge is short-circuited at the end of magnet. But if the distance between the two poles is short enough, the leakage flux through the bridge will be simply from one magnet to another, Fig. 1(e). In such case, Fig. 3(b) shows the lumped magnetic circuit associated with the fluxes excited by $PM1$. However, both Figs. 3(a) and (b) can be simplified into Fig. 3(c) due to symmetry. Similarly, the lumped magnetic circuit associated with the fluxes excited by $PM2$ is shown in Fig. 3(d).

In Fig. 3, ϕ_{g1} and ϕ_{g2} are the air-gap fluxes excited by $PM1$ and $PM2$ over one magnet pole, respectively, while the corresponding reluctances are R_{g1} and R_{g2}. ϕ_{r1} and ϕ_{r2}, and ϕ_{mo1} and ϕ_{mo2} are the flux sources and the leakage fluxes of $PM1$

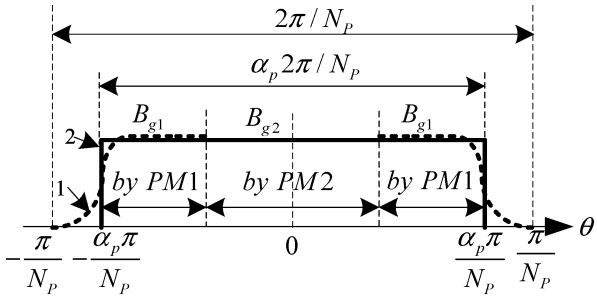

Fig. 2. Equivalent air-gap flux density distribution.

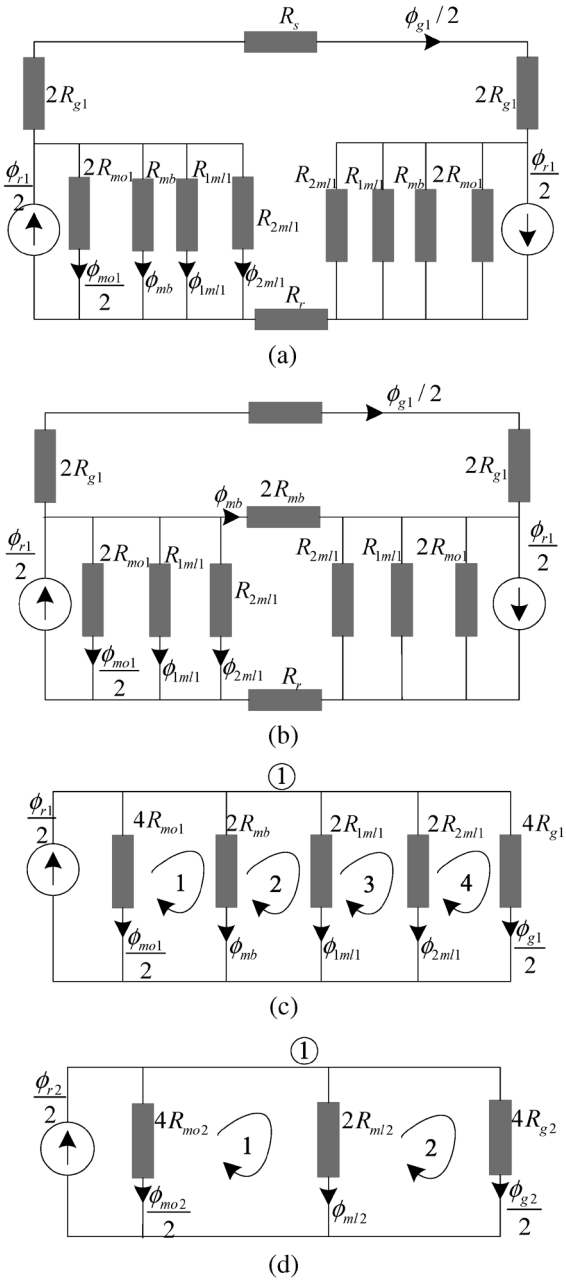

Fig. 3. Lumped magnetic circuits. (a) Lumped magnetic circuit related to $PM1$ in Fig. 1(a). (b) Lumped magnetic circuit related to $PM1$ in Fig. 1(e). (c) Simplified circuit of Fig. 3(a) or Fig. 3(b). (d) Lumped magnetic circuit related to $PM2$.

and $PM2$ over one magnet pole, the corresponding leakage flux reluctances being R_{mo1} and R_{mo2}. ϕ_{mb} is the leakage flux

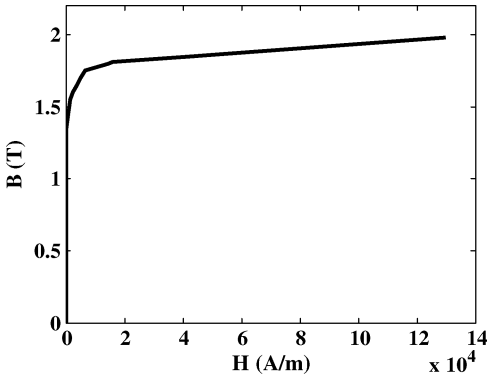

Fig. 4. B-H curve of lamination.

through the bridge, which is represented by the flux line 1 in Fig. 1 and the corresponding reluctance is R_{mb}. ϕ_{1ml1}, ϕ_{2ml1} and ϕ_{ml2} are the magnet end-leakage fluxes, which is represented by the flux lines 2, 3, and 4, and the corresponding reluctances are R_{1ml1}, R_{2ml1} and R_{ml2}. R_r and R_s are the reluctances of the rotor yoke and the stator yoke. In general, there is no significant magnetic saturation in the yokes. Therefore, R_r and R_s may be neglected in comparison with R_{g1} or R_{g2} [5]–[9]. With reference to Fig. 1, the following expressions can be easily obtained:

$$\phi_{r1} = B_r A_{m1} = 2B_r w_{M1} L \tag{1}$$

$$\phi_{r2} = B_r A_{m2} = B_r w_{M2} L \tag{2}$$

$$R_{g1} = g/(\mu_0 A_{g1}) \tag{3}$$

$$R_{g2} = g/\mu_0 (A_g - A_{g1}) \tag{4}$$

$$R_{mo1} = \frac{h_{M1}}{\mu_0 \mu_r A_{m1}} = \frac{h_{M1}}{2\mu_0 \mu_r w_{M1} L} \tag{5}$$

$$R_{mo2} = \frac{h_{M2}}{\mu_0 \mu_r A_{m2}} = \frac{h_{M2}}{\mu_0 \mu_r w_{M2} L} \tag{6}$$

$$R_{1ml1} = \frac{w_b}{\mu_0 L (h_1 + h_2)/2} = \frac{2h_{M1}}{\mu_0 L (h_1 + h_2)} \tag{7}$$

$$R_{2ml1} = \frac{w_b}{\mu_0 L (h_3 + h_4)/2} = \frac{2h_{M1}}{\mu_0 L (h_3 + h_4)} \tag{8}$$

$$R_{ml2} = \frac{2h_{M2}}{\mu_0 L (h_5 + h_6)} \tag{9}$$

$$A_g = \alpha_p \frac{2\pi (R_{i2} - g/2)}{N_P} L \tag{10}$$

where μ_0 is the permeability of air, μ_r is the magnet relative recoil permeability, B_r is the magnet remanence, L is the lamination stack length, g is the air-gap length, and R_{i2} is the stator bore radius. h_{M1} and h_{M2} are magnet length, while w_{M1} and w_{M2} are magnet width. Because of the saturation in the bridge, R_{mb} is nonlinear. But the leakage flux through the bridge can be approximated as [6]–[8]

$$\phi_{mb} \approx B_{sat} A_b \tag{11}$$

where $A_b = bL$ denotes the cross-sectional area of the bridge, b is the bridge width, $B_{\rm sat}$ is the saturation level on the B-H curve of the lamination as shown in Fig. 4, where $B_{\rm sat} = 2$ T. This simplification may cause some errors because of the variation in magnetic saturation level in the bridges under different loading conditions [3], [4]. However, since the bridges are usually designed to be highly saturated even at open-circuit, the accuracy of lumped magnetic circuit models will still be acceptable, as will be illustrated later. Therefore, from Fig. 3(c), the Kirchhoff's law is applied to node ①, and loop 1–4:

$$\begin{pmatrix} 1/2 & 0 & 1 & 1 & 1/2 \\ -R_{mo1} & \phi_{mb} & 0 & 0 & 0 \\ 0 & -\phi_{mb} & R_{1ml1} & 0 & 0 \\ 0 & 0 & -R_{1ml1} & R_{2ml1} & 0 \\ 0 & 0 & 0 & -R_{2ml1} & R_{g1} \end{pmatrix} \begin{pmatrix} \phi_{mo1} \\ R_{mb} \\ \phi_{1ml1} \\ \phi_{2ml1} \\ \phi_{g1} \end{pmatrix} = \begin{pmatrix} \phi_{r1}/2 - \phi_{mb} \\ 0 \\ 0 \\ 0 \\ 0 \end{pmatrix}. \tag{12}$$

It yields the expressions of the leakage fluxes, i.e.,

$$\phi_{mo1} = \frac{(\phi_{r1} - 2\phi_{mb})/R_{mo1}}{1/R_{mo1} + 2/R_{1ml1} + 2/R_{2ml1} + 1/R_{g1}} \tag{13}$$

$$\phi_{1ml1} = \frac{(\phi_{r1} - 2\phi_{mb})/R_{1ml1}}{1/R_{mo1} + 2/R_{1ml1} + 2/R_{2ml1} + 1/R_{g1}} \tag{14}$$

$$\phi_{2ml1} = \frac{(\phi_{r1} - 2\phi_{mb})/R_{2ml1}}{1/R_{mo1} + 2/R_{1ml1} + 2/R_{2ml1} + 1/R_{g1}} \tag{15}$$

$$\phi_{g1} = \frac{(\phi_{r1} - 2\phi_{mb})/R_{g1}}{1/R_{mo1} + 2/R_{1ml1} + 2/R_{2ml1} + 1/R_{g1}}. \tag{16}$$

Therefore, the average air-gap flux density excited by $PM1$ is

$$B_{g1} = \frac{\phi_{g1}}{A_{g1}} = \frac{(\phi_{r1} - 2\phi_{mb})/R_{g1}}{A_{g1}(1/R_{mo1} + 2/R_{1ml1} + 2/R_{2ml1} + 1/R_{g1})}. \tag{17}$$

Similarly, according to Fig. 3(d), the average air-gap flux density excited by $PM2$ is given by

$$B_{g2} = \frac{\phi_{g2}}{A_{g2}} = \frac{\phi_{r2}/R_{g2}}{(A_g - A_{g1})(1/R_{mo2} + 2/R_{ml2} + 1/R_{g2})}. \tag{18}$$

As shown by the curve 1 in Fig. 2, which is the actual air-gap flux density distribution predicted by FEA, B_{g1} and B_{g2} are very similar. Therefore, for simplicity, they are assumed to be equal, i.e.,

$$B_{g1} \approx B_{g2}. \tag{19}$$

Substituting (17) and (18) into (19), the average air-gap flux density is derived:

$$B_{g1} \approx B_{g2} = \frac{\mu_0 (\phi_{r1} - 2\phi_{mb})/g}{1/R_{mo1} + 2/R_{1ml1} + 2/R_{2ml1} + 1/R_{g1}} \tag{20}$$

where

$$\frac{1}{R_{g1}} = \frac{(\phi_{r1} - 2\phi_{mb}) \left(\frac{1}{R_{mo2}} + \frac{2}{R_{ml2}} + \frac{1}{R_g} \right) - \phi_{r2} \left(\frac{1}{R_{mo1}} + \frac{2}{R_{1ml1}} + \frac{2}{R_{2ml1}} \right)}{(\phi_{r1} - 2\phi_{mb}) + \phi_{r2}} \tag{21}$$

$$R_g = \mu_0 A_g / g. \tag{22}$$

Table I lists the design parameters of the prototype machine shown in Fig. 1. Fig. 5 compares the corresponding FEA and

TABLE I
MACHINE DESIGN PARAMETERS

N_P	4	$h_1(mm)$	1.1266	$R_{i2}(mm)$	37.5
α_p	0.6349	$h_2(mm)$	1.8938	$g(mm)$	0.5
$b(mm)$	0.5	$h_3(mm)$	1	$L(mm)$	65
$h_{M1}, h_{M2}(mm)$	3	$h_4(mm)$	2.2426	$B_r(T)$	0.8
$w_{M1}(mm)$	8	$h_5(mm)$	1.1003	$B_{sat}(T)$	2.0
$w_{M2}(mm)$	18	$h_6(mm)$	2.3432	μ_r	1.0667

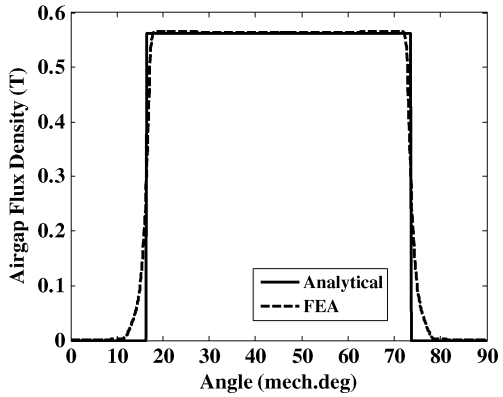

Fig. 5. Comparison of predicted air-gap flux density distributions.

TABLE II
AVERAGE AIR-GAP FLUX DENSITY (T)

Parameters		$B_g(T)$ FEA B_{g1}	FEA B_{g2}	Analytical $B_{g1} \approx B_{g2}$	Error (%) B_{g1}	Error (%) B_{g2}
$h_{M1}(mm)$	3 2	0.5425	0.5410	0.5397	0.52	0.24
	3 3	0.5654	0.5633	0.5624	0.53	0.16
$h_{M2}(mm)$	3 4	0.5766	0.5751	0.5731	0.61	0.35
	3 5	0.5827	0.5811	0.5784	0.74	0.46
	4 5	0.5947	0.5932	0.5926	0.35	0.10
$b(mm)$	0.6	0.5581	0.5568	0.5539	0.75	0.52
	0.5	0.5654	0.5633	0.5624	0.53	0.16
	0.4	0.5726	0.5710	0.5709	0.3	0.02
α_p	0.7356	0.4960	0.4943	0.4939	0.42	0.08
	0.6349	0.5654	0.5633	0.5624	0.53	0.16
	0.5263	0.6540	0.6527	0.6571	0.47	0.67
$w_{M1}(mm)$	6	0.4946	0.4933	0.4915	0.63	0.36
	8	0.5654	0.5633	0.5624	0.53	0.16
	10	0.6357	0.6339	0.6332	0.39	0.11
$w_{M2}(mm)$	16	0.5301	0.5286	0.5269	0.6	0.32
	18	0.5654	0.5633	0.5624	0.53	0.16
	20	0.5994	0.5982	0.5978	0.27	0.07
$\sum_{i=1}^{6} h_i(mm)$	16.3350	0.5513	0.5496	0.5488	0.45	0.14
	9.6068	0.5654	0.5633	0.5624	0.53	0.16
	7.0994	0.5708	0.5694	0.5699	0.16	0.09

analytically predicted results, while Table II shows further comparison between the FEA and analytically predicted results for different b, α_p, w_{M1}, w_{M2}, h_{M1}, h_{M2} and $\sum_{i=1}^{6} h_i$. As can be seen, the errors are small and $<1\%$.

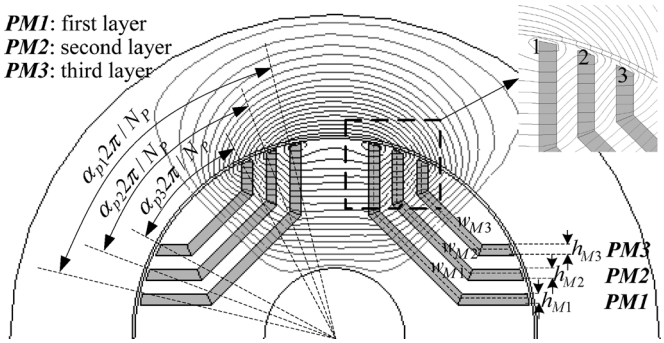

Fig. 6. IPM machine structure with multilayer permanent magnets.

III. ANALYTICAL MODEL FOR MULTILAYER IPM MACHINES

Fig. 6 shows the FEA predicted flux distribution of an IPM machine with three-layer permanent magnets, designated as $PM1$, $PM2$ and $PM3$, respectively. The air-gap cross-sectional area can be divided in three parts:

$$A_{g1} = (\alpha_{p1} - \alpha_{p2}) \frac{2\pi(R_{i2} - g/2)}{N_P} L \tag{23}$$

$$A_{g2} = (\alpha_{p2} - \alpha_{p3}) \frac{2\pi(R_{i2} - g/2)}{N_P} L \tag{24}$$

$$A_{g2} = \alpha_{p3} \frac{2\pi(R_{i2} - g/2)}{N_P} L. \tag{25}$$

According to the paths of flux lines in Fig. 6, it shows that the flux lines through A_{g1} are only excited by $PM1$. The flux lines through A_{g2} are excited by both $PM1$ and $PM2$, while the flux lines through A_{g3} are excited by $PM1$, $PM2$ and $PM3$. In Fig. 6, the leakage flux through the bridge at $PM1$, which is represented by the flux line 1, is only excited by $PM1$, because its path is only through $PM1$ and the bridge. However, the leakage flux of the bridge at $PM2$ is much different. It is excited by $PM1$ and part of $PM2$, passes through the bridge and then into the air gap, as shown by the flux line 2 in Fig. 6. But it can be divided into two parts. One part is the leakage flux through the bridge excited by $PM2$ only, and the remaining part is the flux into the air gap excited by $PM1$. Similarly, the leakage flux of the bridge at $PM3$ can also be divided into the leakage flux excited by $PM3$ and the air-gap flux excited by $PM1$ and $PM2$. Therefore, the actual air-gap flux density distribution, curve 1 in Fig. 7, can be simplified by curve 2.

From the foregoing analysis, the derived lumped magnetic circuit is shown in Fig. 8(a). In Fig. 6(a), ϕ_{r1}, ϕ_{r2}, and ϕ_{r3} are the flux sources of $PM1$, $PM2$ over one magnet pole:

$$\phi_{r1} = B_r A_{m1} = B_r w_{M1} L \tag{26}$$

$$\phi_{r2} = B_r A_{m2} = B_r w_{M2} L \tag{27}$$

$$\phi_{r3} = B_r A_{m3} = B_r w_{M3} L \tag{28}$$

where w_{M1}, w_{M2}, and w_{M3} are the average magnet width. ϕ_{mo1}, ϕ_{mo2}, and ϕ_{mo3} are the leakage fluxes of $PM1$, $PM2$, and $PM3$ over one magnet pole, and the corresponding

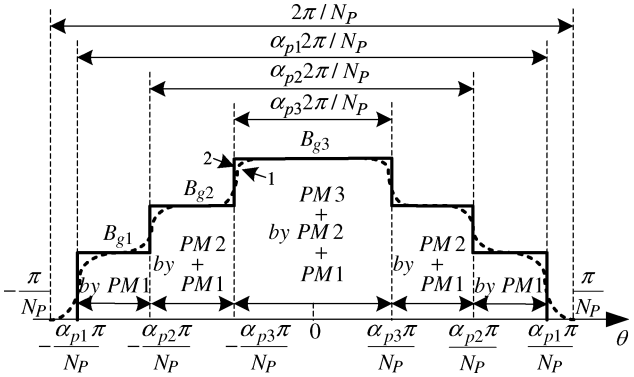

Fig. 7. Equivalent air-gap flux density distribution.

reluctances are

$$R_{mo1} = \frac{h_{M1}}{\mu_0 \mu_r A_{m1}} = \frac{h_{M1}}{\mu_0 \mu_r w_{M1} L} \tag{29}$$

$$R_{mo2} = \frac{h_{M2}}{\mu_0 \mu_r A_{m2}} = \frac{h_{M2}}{\mu_0 \mu_r w_{M2} L} \tag{30}$$

$$R_{mo3} = \frac{h_{M3}}{\mu_0 \mu_r A_{m3}} = \frac{h_M}{\mu_0 \mu_r w_{M3} L}. \tag{31}$$

h_{M1}, h_{M2}, and h_{M3} are the magnet lengths of different PM layers. ϕ_{g1}, ϕ_{g2}, and ϕ_{g3} are the fluxes passing through the areas A_{g1}, A_{g2}, and A_{g3}, respectively. Therefore, the corresponding reluctances are $R_{g1} = g/(\mu_0 A_{g1})$, $R_{g2} = g/(\mu_0 A_{g2})$, and $R_{g3} = g/(\mu_0 A_{g3})$. ϕ_{mb1}, ϕ_{mb2}, and ϕ_{mb3} are the leakage fluxes through the bridge at $PM1$, $PM2$, and $PM3$, respectively, and $\phi_{mb1} \approx B_{sat} b_1 L$, $\phi_{mb2} \approx B_{sat} b_2 L$, and $\phi_{mb2} \approx B_{sat} b_3 L$. b_1, b_2, and b_3 are the bridge widths, and R_{mb1}, R_{mb2}, and R_{mb3} are the corresponding reluctances. R_{s1}, R_{s2}, R_{s3}, and R_r are the reluctances of the rotor yoke and the stator yoke. Similar to the assumptions mentioned in Section II, neglecting the magnetic saturation in both stator and rotor yokes leads to negligible values of R_{s1}, R_{s2}, R_{s3}, and R_r [5]–[9]. Therefore, Fig. 8(a) can be simplified to Fig. 8(b). Using the same method as in Section II, the Kirchhoff's law is applied to node ① − ③, and loop 1–6:

$$\phi_{mo3}/2 + \phi_{g3}/2 = \phi_{r3}/2 - \phi_{mb3} \tag{32}$$

$$\phi_{mo2}/2 + \phi_{g2}/2 - \phi_{mo3}/2 = \phi_{r2}/2 - \phi_{mb2} - \phi_{r3}/2 + \phi_{mb3} \tag{33}$$

$$\phi_{mo2}/2 + \phi_{g1}/2 - \phi_{mo2}/2 = \phi_{r1}/2 - \phi_{mb1} - \phi_{r2}/2 + \phi_{mb2} \tag{34}$$

$$\phi_{mb3} R_{mb3} - \phi_{mo3} R_{mo3} = 0 \tag{35}$$

$$\phi_{mb2} R_{mb2} - \phi_{mo2} R_{mo2} = 0 \tag{36}$$

$$\phi_{mb1} R_{mb1} - \phi_{mo1} R_{mo1} = 0 \tag{37}$$

$$\phi_{g1} R_{g1} - \phi_{mb1} R_{mb1} = 0 \tag{38}$$

$$\phi_{g2} R_{g2} - \phi_{g1} R_{g1} - \phi_{mb2} R_{mb2} = 0 \tag{39}$$

$$\phi_{g3} R_{g3} - \phi_{g2} R_{g2} - \phi_{mb3} R_{mb3} = 0. \tag{40}$$

ϕ_{mo1}, ϕ_{mo2}, ϕ_{mo3}, ϕ_{g1}, ϕ_{g2}, and ϕ_{g3} can be easily obtained from (32)–(40). Then, the average air-gap flux densities which are shown in Fig. 7 are $B_{g1} = \phi_{g1}/A_{g1}$, $B_{g2} = \phi_{g2}/A_{g2}$, and $B_{g3} = \phi_{g3}/A_{g3}$, respectively.

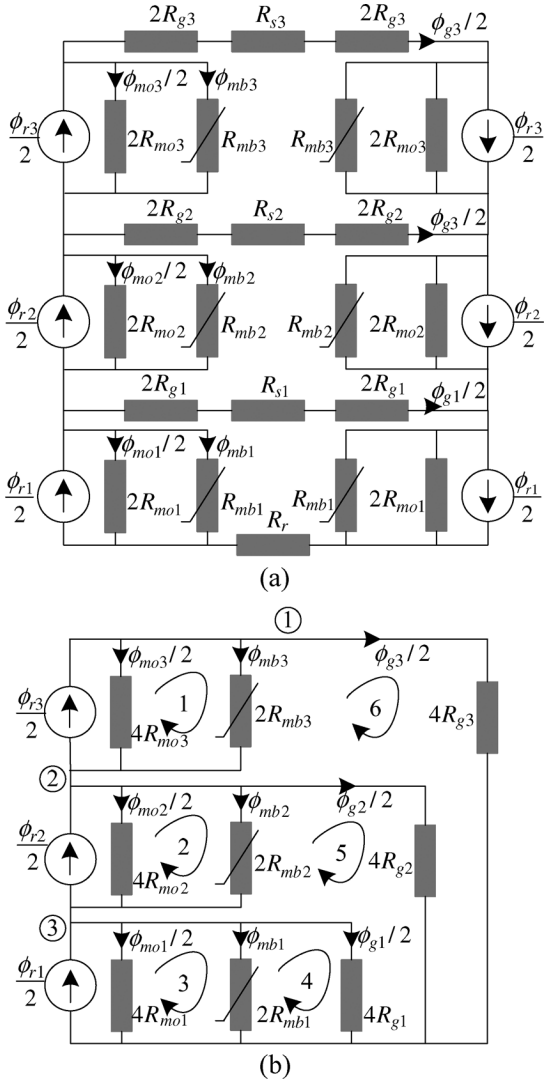

Fig. 8. Lumped magnetic circuit for three-layer IPM machine. (a) Lumped magnetic circuit for Fig. 6. (b) A simplified form of Fig. 6(a).

TABLE III
MACHINE DESIGN PARAMETERS

N_P	4	$B_r(T)$	0.8	$w_{M1}(mm)$	56.4525
α_{p1}	0.8724	$B_{sat}(T)$	2.0	$w_{M2}(mm)$	47.7542
α_{p2}	0.7164	$R_{i2}(mm)$	37.5	$w_{M3}(mm)$	37.8709
α_{p3}	0.5560	$L(mm)$	65	$h_{M1}, h_{M2}, h_{M3}(mm)$	2
μ_r	1.0667	$g(mm)$	0.5	$b_1, b_2, b_3(mm)$	0.5

Table III lists the design parameters of the prototype machine shown in Fig. 6. Fig. 11 and Table IV compare the FEA and analytically predicted results. Excellent agreement is again achieved.

Therefore, from the above method, it is shown that for the IPM machine with three-layer permanent magnets, the air-gap cross-sectional area can be divided into three parts where the fluxes are excited by $PM1$, $PM1 + PM2$ and $PM1 + PM2 + PM3$, respectively. Meanwhile, the leakage fluxes through the bridges at different PMs are separately supplied by $PM1$, $PM2$, and $PM3$. Similarly, the lumped

TABLE IV
AVERAGE AIR-GAP FLUX DENSITY FOR THREE-LAYER MACHINE

	FEA results	Analytical results	Error (%)
B_{g1}	0.4218	0.4192	0.62
B_{g2}	0.6653	0.6688	0.53
B_{g3}	0.8085	0.8222	1.69

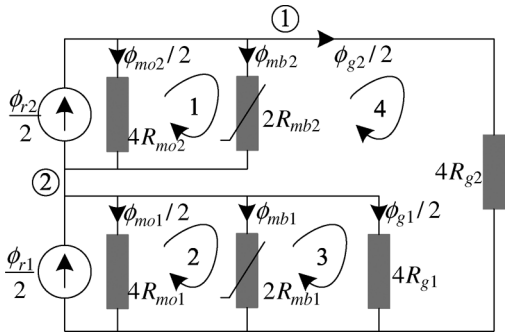

Fig. 9. Lumped magnetic circuit for two-layer IPM machine.

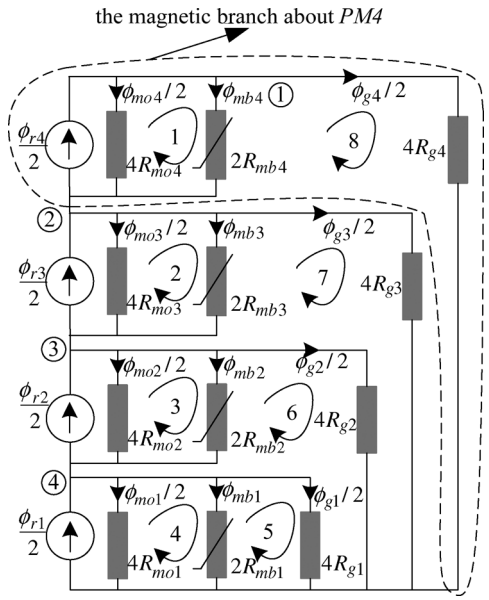

Fig. 10. Lumped magnetic circuit for four-layer IPM machine.

magnetic circuits for the IPM machine with two-layer PMs and four-layer PMs can be derived, as shown in Figs. 9 and 10. Figs. 12 and 13, Tables V and VI compare the FEA and analytically predicted results for the two-layer and the four-layer IPM machines. The errors are all $<2\%$.

By using the same method, the air-gap cross-sectional area of the $(n+1)$-layer IPM machine can be divided into $(n+1)$ parts:

$$A_{g(k)} = \left(\alpha_{p(k)} - \alpha_{p(k-1)}\right) \frac{2\pi(R_{i2} - g/2)}{N_P} L \quad (k = 1, 2, \ldots, n-1) \tag{41}$$

$$A_{gn} = \alpha_{pn} \frac{2\pi(R_{i2} - g/2)}{N_P} L. \tag{42}$$

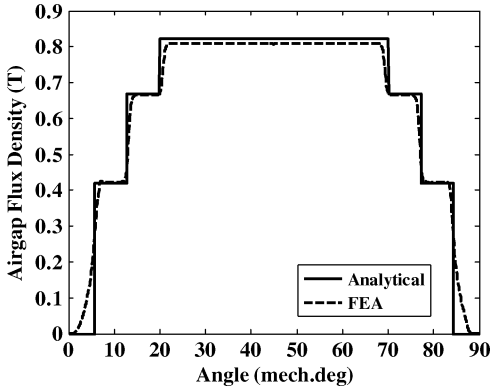

Fig. 11. Air-gap flux density distribution of three-layer IPM machine.

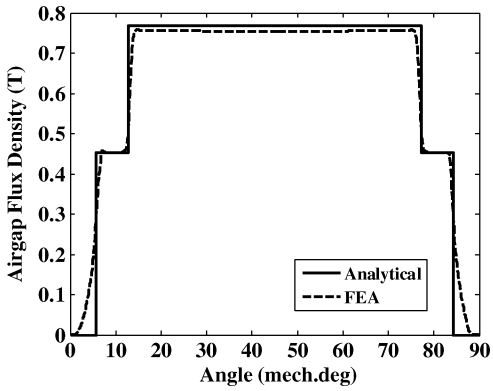

Fig. 12. Air-gap flux density distribution of two-layer IPM machine.

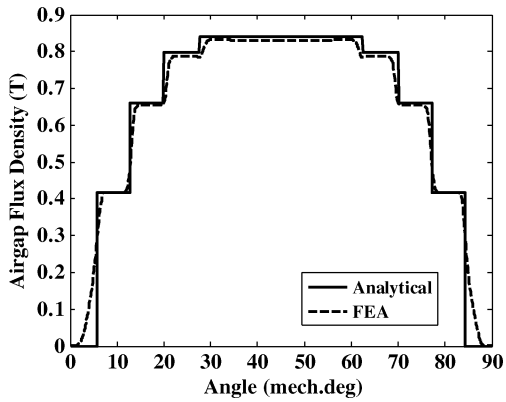

Fig. 13. Air-gap flux density distribution of four-layer IPM machine.

TABLE V
AVERAGE AIR-GAP FLUX DENSITY FOR TWO-LAYER MACHINE

	FEA results	Analytical results	Error (%)
B_{g1}	0.4532	0.4535	0.07
B_{g2}	0.7546	0.7681	1.79

The flux through $A_{g(k)}$ is excited by $\sum_{i=1}^{k} PM(i)$. Then, the lumped magnetic circuit of the $(n+1)$-layer IPM machine can be derived from the circuit of the n-layer IPM machine by adding a magnetic branch about the $(n+1)$th layer in parallel with the lumped magnetic circuit of the n-layer IPM machine.

TABLE VI
AVERAGE AIR-GAP FLUX DENSITY FOR TWO-LAYER MACHINE

	FEA results	Analytical results	Error (%)
B_{g1}	0.4173	0.4163	0.24
B_{g2}	0.6554	0.6601	0.72
B_{g3}	0.7873	0.7983	1.4
B_{g4}	0.8309	0.8393	1.01

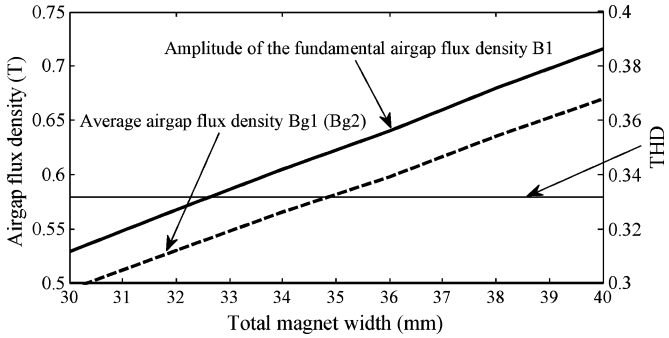

Fig. 14. Influence of magnet width on air-gap flux density ($\alpha_p = 0.6349$).

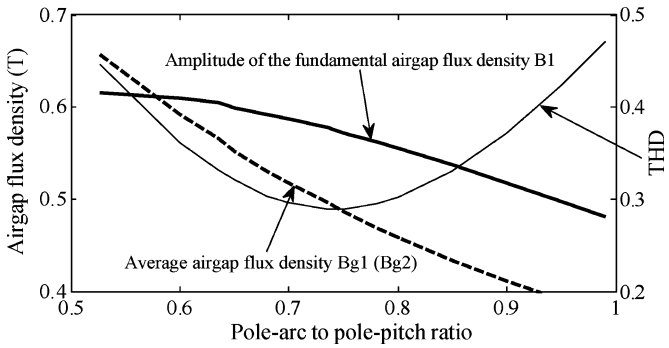

Fig. 15. Influence of pole-arc to pole-pitch ratio on air-gap flux density ($w_M = 34$ mm).

IV. OPTIMIZATION WITH ANALYTICAL MODEL

In order to achieve high torque density, high efficiency, and low torque ripple, it is desirable to maximize the fundamental air-gap flux density and minimize the THD of air-gap flux density. The EMF waveform is directly related to the air-gap field distribution and the winding configuration. Particularly, if the windings are concentrated and fully pitched, the EMF waveform will be identical to the air-gap field distribution. Therefore, the optimization of air-gap flux density is an important design issue. With the developed lumped magnetic circuit models, such optimization is much easier than that with FEA.

A. Optimization of Multisegment IPM Machines

For the prototype multisegmented IPM machine in Table I, α_p, w_{M1}, or w_{M2} can be optimized for maximum peak fundamental air-gap flux density or minimum THD of air-gap flux density with the lumped magnetic circuit model. In Fig. 14, B_1 is the amplitude of the fundamental component of the air-gap flux density B_{g1}. Total magnet width is $w_M = 2w_{M1} + w_{M2}$, which represents the magnet volume. If the pole-arc to pole-pitch ratio remains constant, B_{g1} and B_1 increases with the increase of magnet volume, but the THD remains constant, as shown in Fig. 14. If the magnet volume remains constant, the air-gap flux density and its amplitude of the fundamental component decrease as the pole-arc to pole-pitch ratio is increased, Fig. 15. In Fig. 16, the magnet width and α_p are increased in order to obtain the same air-gap flux density B_{g1}. It can be seen from Fig. 16, if B_{g1} remains constant, B_1 will increase with α_p, while THD variation in Fig. 16 is exactly the same as that in Fig. 15, which indicates that THD is only related to α_p. Clearly, there is an optimal pole-arc to pole-pitch ratio, viz. $\alpha_p = 0.75$, for minimum THD. When $\alpha_p = 0.75$ and $w_M = 36$ mm, the cross section of the rotor and corresponding air-gap field distribution are shown in Fig. 17. Table VII compares FEA and analytically predicted results. They have very good agreement.

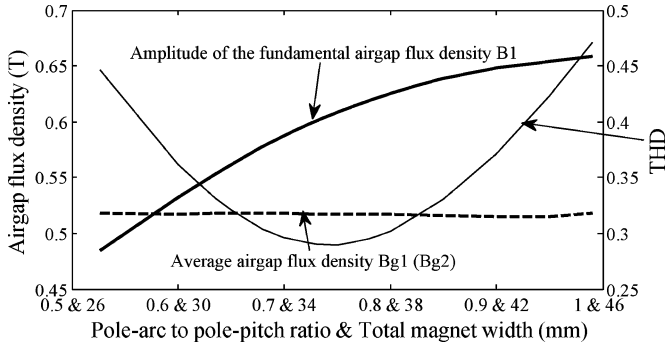

Fig. 16. Influence of pole-arc to pole-pitch ratio and total magnet width on air-gap flux density.

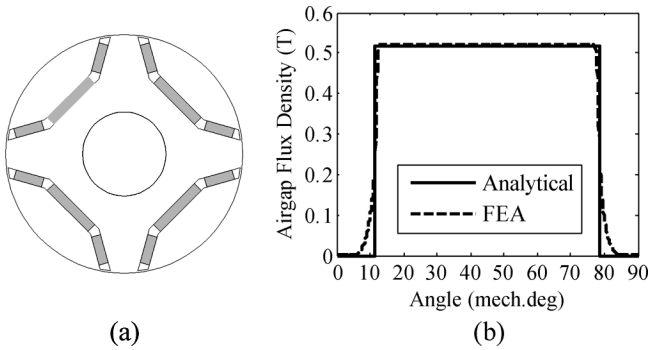

Fig. 17. Optimized multisegment IPM machine. (a) Rotor. (b) Air-gap field distribution.

TABLE VII
COMPARISON OF FEA AND ANALYTICALLY PREDICTED RESULTS OF OPTIMIZED MULTISEGMENT IPM MACHINE

	FEA	Analytical	Error (%)
B_{g1}	0.5224	0.5176	0.98
B_{g2}	0.5209	0.5173	0.69
B_1 (T)	0.6138	0.6085	0.86
THD (%)	25.52	28.97	3.45

B. Optimization of Multilayer IPM Machines

For the prototype multilayer IPM machine in Table III, the influence of number of PM layers and displacement of different

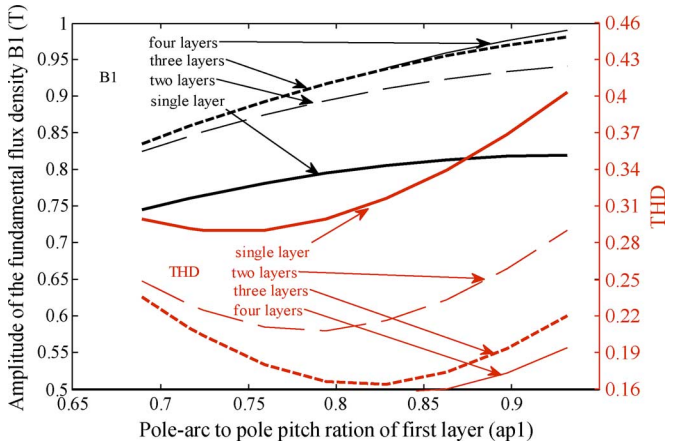

Fig. 18. Influence of number of PM layers on air-gap flux density.

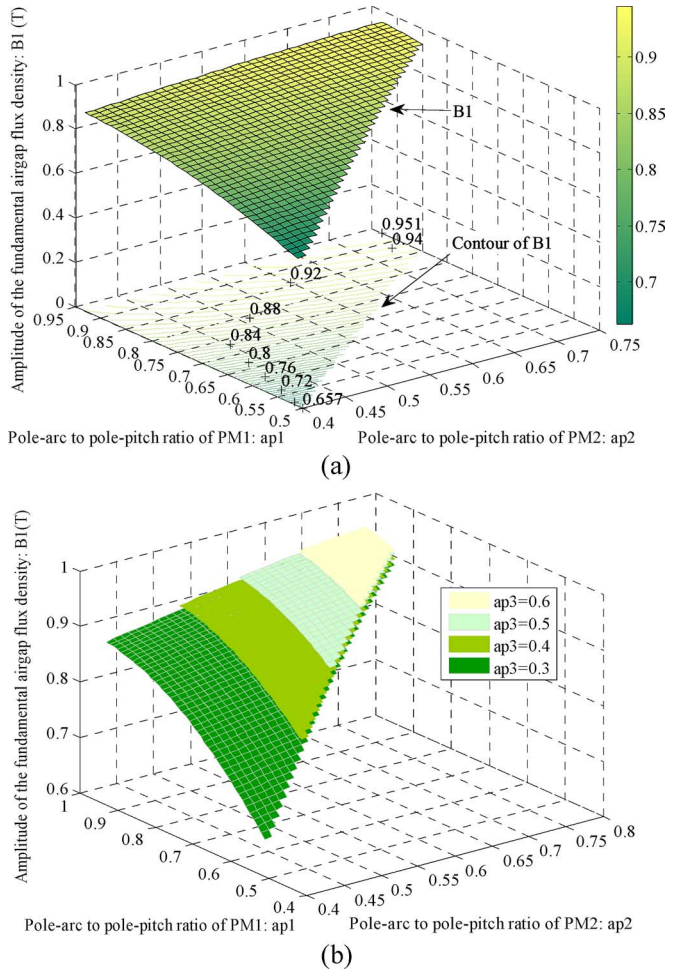

Fig. 19. Influence of displacement of three layers on amplitude of the fundamental air-gap flux density. (a) $\alpha_{p3} = 0.3$; (b) with different α_{p3}.

layers is investigated and optimized for maximum fundamental air-gap flux density or minimum THD of air-gap flux density, as shown in Figs. 18–21. The three-layer IPM machine in Fig. 18 is obtained from the four-layer PM machine without the fourth PM layer, similarly for the two and single-layer IPM machine. It can be seen from Fig. 18 that the amplitude of the fundamental air-gap flux density of the two-layer machine is significantly higher than that of single-layer machine, because of the increase of magnet volume, while the THD of air-gap flux density of two-layer machine is significantly lower than that of single-layer machine, since the air-gap field distribution becomes closer to sine waveform rather than the rectangular waveform. Therefore, for brushless dc machines with rectangular input current, single-layer is better for its rectangular air-gap flux density. But for brushless ac machines, multilayer is a better choice for its more sinusoidal air-gap flux distribution. However, with further increase of the number of PM layers, the benefits in both fundamental air-gap field and THD gradually diminish, as can be seen for the three-layer and four-layer IPM machines in Fig. 18. Therefore, for the prototype machine, three-layer PM rotor may be preferred. For the three-layer IPM machine, the influence of displacement of different layers is investigated, Figs. 19–21. It shows with the increasing of α_{p1}, α_{p2}, or α_{p3}, the amplitude of the fundamental air-gap flux density increases because of more magnet volume. From the contour of the amplitude of the fundamental air-gap flux density in Fig. 19(a), the influence of α_{p1} is bigger than that of α_{p2} on B_1, and the influence of α_{p3} is even smaller, Fig. 19(b). THD variation is more complex with different combination of α_{p1}, α_{p2} or α_{p3}. In Fig. 20, with various specified α_{p3}, both α_{p1} and α_{p2} have optimal range of values for minimum THD. With the increase of α_{p3}, the optimal range of both α_{p1} and α_{p2} gradually increases, as shown in Fig. 20 and summarized in Table VIII. It is because for the air-gap flux density being close to sine and not to rectangular waveform, the values of α_{p1}, α_{p2}, or α_{p3} should not be too close to each other. Furthermore, from the contour of THD in Fig. 20, the influence of α_{p1} on THD is most significant, while the influence of α_{p3} is smallest. In Fig. 20 and Table VIII, with the increase of α_{p3} from 0.3 to 0.4, the THD obviously reduces, but from 0.4 to 0.5, the effect is very little. With further increase of α_{p3}, THD does not decrease but increase, as shown in Fig. 20(d) and Table VIII. To find the optimal range of α_{p3}, minimum THD with different α_{p1}, α_{p2} is obtained for various specified α_{p3}. Then, the variation of minimum THD in Fig. 20 with α_{p3} is shown in Fig. 21. Similar to Fig. 20, when α_{p3} is from 0.4 to 0.5, the THD is small. Clearly, there are optimal pole-arc to pole-pitch ratios, viz. $\alpha_{p1} = 0.83$, $\alpha_{p2} = 0.6$, and $\alpha_{p3} = 0.45$, for minimum THD. When the pole-arc to pole-pitch ratios of PM1, PM2, and PM3 are 0.83, 0.6, and 0.45, respectively, the cross section of the rotor and corresponding air-gap field distribution are shown in Fig. 22. Table IX compares FEA and analytically predicted results. They have very good agreement.

V. Conclusion

Lumped magnetic circuit models for interior permanent magnet (IPM) machines with multisegment and multilayer permanent magnets have been developed for analytically predicting the open-circuit air-gap field distribution, average air-gap flux density and leakage fluxes. The FEA is adopted to verify the developed models and analytical method. It shows that for the prototype machines, the errors between the FEA results and analytical predictions are $<1\%$ for multisegment IPM machines and $<2\%$ for multilayer IPM machines. By utilizing the developed lumped magnetic circuit models, the

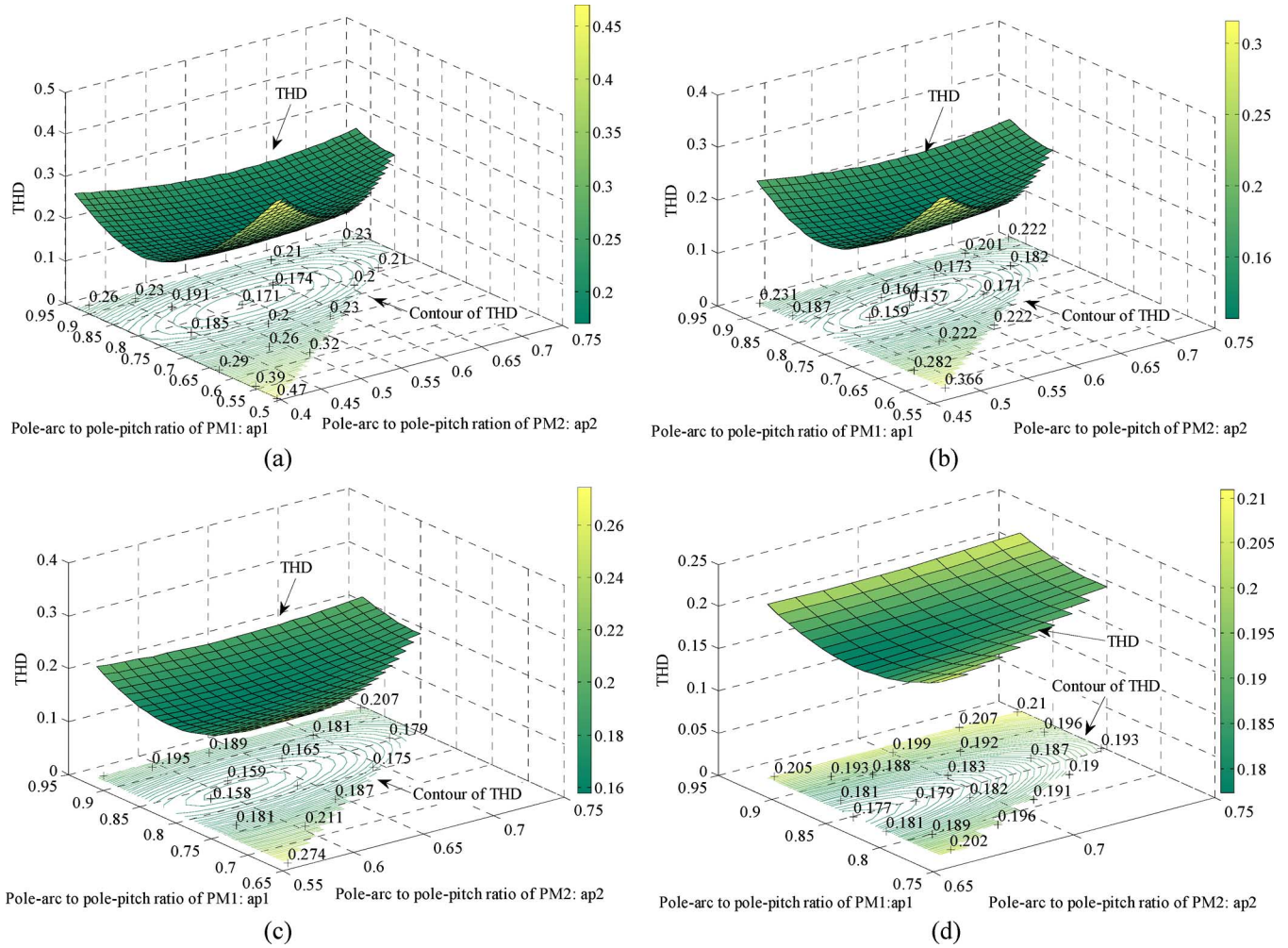

Fig. 20. Influence of displacement of three layers on THD of air-gap flux density. (a) $\alpha_{p3} = 0.3$; (b) $\alpha_{p3} = 0.4$; (c) $\alpha_{p3} = 0.5$; (d) $\alpha_{p3} = 0.6$.

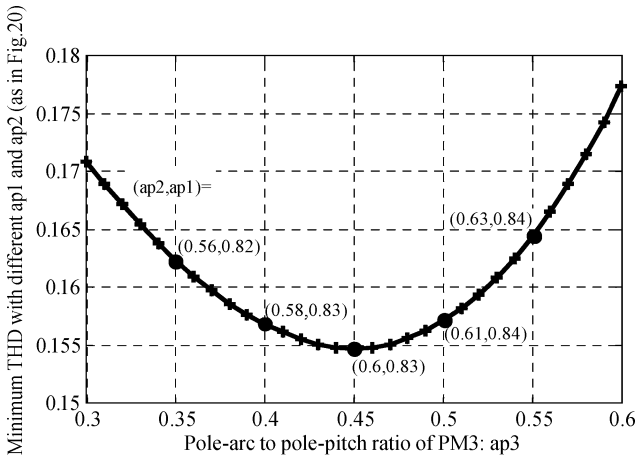

Fig. 21. THD optimization.

IPM machines are optimized for maximum fundamental and minimum THD of air-gap flux density waveform.

Of course, many other design issues should also be considered, e.g., the saliency ratio. Nevertheless, the developed analytical models can be used for calculating the back-EMF waveforms and optimal air-gap field distribution with minimum THD

TABLE VIII
OPTIMAL VALUES OF α_{p1} AND α_{p2} AT DIFFERENT α_{p3} FOR SMALL THD ACCORDING TO Fig. 20

α_{p3}	0.3	0.4	0.5	0.6
α_{p2}	0.5~0.6	0.53~0.63	0.57~0.65	0.66~0.68
α_{p1}	0.78~0.84	0.8~0.85	0.81~0.86	0.83~0.87
min THD	0.171	0.157	0.158	0.177

in IPM machines with multisegment and multilayer permanent magnets and should be beneficial for the IPM machine design.

Currently, the paper is restricted to analytical modeling of open-circuit air-gap field distribution in IPM machines. On load, the magnetic field will be more complex, e.g., (a) the armature reaction field will change with the load condition and rotor position; (b) reluctance of the stator yoke and teeth cannot be neglected; (c) the magnetic saturation level, particularly in the rotor iron and bridge, will vary with the load; (d) the cross-coupling magnetic saturation between the d- and q-axes under different load angle will be significant [28]. Therefore, on load it is more difficult to analytically derive the air-gap field distribution in IPM machines. However, since the developed model is based

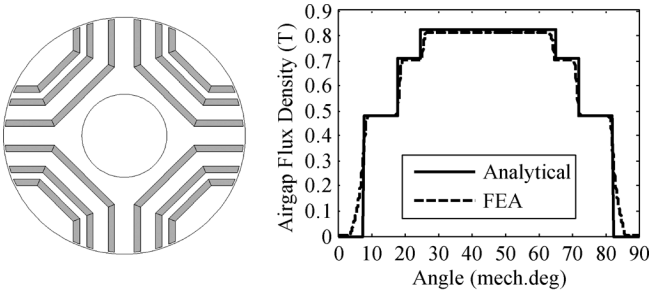

Fig. 22. Optimized multilayer IPM machine. (a) Rotor. (b) Air-gap field distribution.

TABLE IX
COMPARISON OF FEA AND ANALYTICALLY PREDICTED RESULTS OF OPTIMIZED MULTILAYER IPM MACHINE

	FEA	Analytical	Error (%)
B_{g1}	0.4784	0.4780	0.08
B_{g2}	0.7041	0.7110	0.98
B_{g3}	0.8113	0.8268	1.91
B_1 (T)	0.9057	0.9228	1.89
THD (%)	12.78	15.48	2.7

on the lumped magnetic circuit model, it can be extended, similar to [3]–[9], to accounting for the nonlinear magnetic property of stator yoke and teeth, rotor irons, bridges and yoke, etc., together with the effect of stator slotting and armature current, which is being carried out and will be reported in a future paper.

REFERENCES

[1] T. J. E. Miller, *Brushless Permanent-Magnet and Reluctance Motor Drives*. New York: Oxford University Press, 1989.
[2] T. M. Jahns and V. Blasko, "Recent advances in power electronics technology for industrial and traction machine drives," *Proc. IEEE*, vol. 89, no. 6, pp. 963–975, Jun. 2001.
[3] C. Mi, M. Filippa, W. Liu, and R. Q. Ma, "Analytical method for predicting the air-gap flux of interior-type permanent-magnet machines," *IEEE Trans. Magn.*, vol. 40, no. 1, pp. 50–58, Jan. 2004.
[4] S. H. Han, T. M. Jahns, and W. L. Soong, "A magnetic circuit model for an IPM synchronous machine incorporating moving arigap and cross-coupled saturation effects," in *Proc. IEEE Int. Electric Machines and Drives Conf. (IEMDC)*, May 3–5, 2007, pp. 21–26.
[5] N. Matsui, M. Nakamura, and T. Kosaka, "Instantaneous torque analysis of hybrid stepping motor," *IEEE Trans. Ind. Appl.*, vol. 32, no. 5, pp. 1176–1182, 1996.
[6] W. B. Tsai and T. Y. Chang, "Analysis of flux leakage in a brushless permanent-magnet motor with embedded magnets," *IEEE Trans. Magn.*, vol. 35, no. 1, pp. 543–547, Jan. 1999.
[7] C. C. Hwang and Y. H. Cho, "Effects of leakage flux on magnetic fields of interior permanent magnet synchronous motors," *IEEE Trans. Magn.*, vol. 37, no. 4, pp. 3021–3024, Jul. 2001.
[8] E. C. Lovelace, T. M. Jahns, and J. H. Lang, "A saturating lumped parameter model for an interior PM synchronous machine," *IEEE Trans. Ind. Appl.*, vol. 38, no. 3, pp. 645–650, 2002.
[9] M. A. Rahman, T. A. Little, and G. R. Slemon, "Analytical models for interior-type permanent magnet synchronous motors," *IEEE Trans. Magn.*, vol. MAG-21, no. 5, pp. 1741–1743, Sep. 1985.
[10] Z. Q. Zhu, D. Howe, E. Bolte, and B. Ackermann, "Instantaneous magnetic field distribution in brushless permanent magnet dc motors, part I: Open-circuit field," *IEEE Trans. Magn.*, vol. 29, no. 1, pp. 124–135, Jan. 1993.
[11] Z. Q. Zhu, D. Howe, and C. C. Chan, "Improved analytical model for predicting the magnetic field distribution in brushless permanent-magnet machines," *IEEE Trans. Magn.*, vol. 38, no. 1, pp. 229–238, Jan. 2002.
[12] Z. Q. Zhu, D. Howe, and Z. P. Xia, "Prediction of open-circuit airgap field distribution in brushless machines having an inset permanent magnet rotor topology," *IEEE Trans. Magn.*, vol. 30, no. 1, pp. 98–107, Jan. 1994.
[13] D. Zarko, D. Ban, and T. A. Lipo, "Analytical calculation of magnetic field distribution in the slotted air gap of a surface permanent-magnet motor using complex relative air-gap permeance," *IEEE Trans. Magn.*, vol. 42, no. 7, pp. 1828–1837, Jul. 2006.
[14] Z. Q. Zhu and D. Howe, "Instantaneous magnetic field distribution in brushless permanent magnet dc motors, part III: Effect of stator slotting," *IEEE Trans. Magn.*, vol. 29, no. 1, pp. 143–151, Jan. 1993.
[15] D. Zarko, D. Ban, and T. A. Lipo, "Analytical solution for cogging torque in surface permanent-magnet motors using conformal mapping," *IEEE Trans. Magn.*, vol. 44, no. 1, pp. 52–65, Jan. 2008.
[16] A. Kiyoumarisi, M. R. Hassanzadeh, and M. Moallem, "A new analytical method on the field calculation of interior permanent-magnet synchronous motors," *Scientica Iranica*, vol. 13, no. 4, pp. 364–372, 2006.
[17] F. Liang, S. O. Kwon, and J. P. Hong, "Conformal transformation technique for prediction of the magnetic field distribution in an IPM motor," in *Proc. Eighth Int. Conf. Electrical Machines and Systems (ICEMS)*, 2005, vol. 3, pp. 2124–2128.
[18] R. Qu and T. A. Lipo, "Analysis and modeling of air-gap and zigzag leakage fluxes in a surface-mounted permanent-magnet machine," *IEEE Trans. Ind. Appl.*, vol. 40, no. 1, pp. 121–127, 2004.
[19] J. P. Wang, D. K. Lieu, W. L. Lorimer, and A. Hartman, "Comparison of lumped parameter and finite element magnetic modeling in a brushless DC motor," *IEEE Trans. Magn.*, vol. 33, no. 5, pp. 4092–4094, Sep. 1997.
[20] Y. Kano, T. Kosaka, and N. Matsui, "Simple nonlinear magnetic analysis for permanent-magnet motors," *IEEE Trans. Ind. Appl.*, vol. 41, no. 5, pp. 1205–1214, 2005.
[21] M. Moallen and G. E. Dawson, "An improved magnetic equivalent circuit method for predicting the characteristics of highly saturated electromagnetic devices," *IEEE Trans. Magn.*, vol. 34, no. 5, pp. 3632–3635, Sep. 1998.
[22] J. K. Kim, S. W. Joo, S. C. Hahn, J. P. Hong, D. H. Kang, and D. H. Koo, "Static characteristics of linear BLDC motor using equivalent magnetic circuit and finite element method," *IEEE Trans. Magn.*, vol. 40, no. 2, pp. 742–745, Mar. 2004.
[23] K. Shima, K. Ide, M. Takahashi, and K. Oka, "Steady-state magnetic circuit analysis of salient-pole synchronous machines considering cross-magnetization," *IEEE Trans. Energy Convers.*, vol. 18, no. 2, pp. 213–218, 2003.
[24] Z. Q. Zhu, Y. Pang, D. Howe, S. Iwasaki, R. Deodhar, and A. Pride, "Analysis of electromagnetic performance of flux-switching permanent-magnet machines by nonlinear adaptive lumped parameter magnetic circuit model," *IEEE Trans. Magn.*, vol. 41, no. 11, pp. 4277–4287, Nov. 2005.
[25] Y. Chen, Z. Q. Zhu, and D. Howe, "3-D lumped parameter magnetic circuit analysis of single-phase flux-switching permanent magnet motor," *IEEE Trans. Ind. Appl.*, vol. 44, no. 6, pp. 1701–1710, 2008.
[26] M. Cheng, K. T. Chau, C. C. Chan, E. Zhou, and X. Huang, "Nonlinear varying-network magnetic circuit analysis for doubly salient permanent-magnet motors," *IEEE Trans. Magn.*, vol. 36, no. 1, pp. 339–348, Jan. 2000.
[27] D. C. Hanselman, *Brushless Permanent-Magnet Motor Design*. New York: McGraw-Hill, 1994.
[28] G. Qi, J. T. Chen, Z. Q. Zhu, D. Howe, L. B. Zhou, and C. L. Gu, "Influence of skew and cross-coupling on flux-weakening performance of PM brushless AC machines," *IEEE Trans. Magn.*, vol. 45, no. 5, pp. 2110–2117, May 2009.